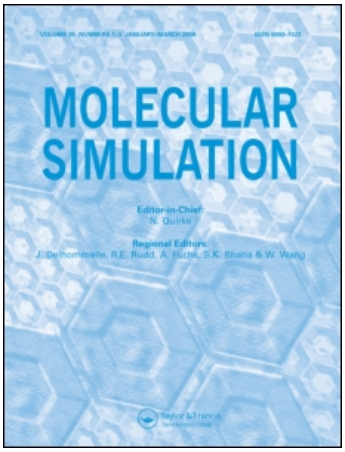

Molecular Simulation
Publication details, including instructions for authors and subscription information:
http://www.informaworld.com/smpp/title~content=t713644482

A lattice kinetic Monte Carlo study of void morphological evolution during silicon crystal growth

J. Dai[a]; W. D. Seider[a]; T. Sinno[a]
[a] Department of Chemical and Biomolecular Engineering, University of Pennsylvania, Philadelphia, PA, USA

To cite this Article Dai, J. , Seider, W. D. and Sinno, T.(2007) 'A lattice kinetic Monte Carlo study of void morphological evolution during silicon crystal growth', Molecular Simulation, 33: 9, 733 — 745
To link to this Article: DOI: 10.1080/08927020701310915
URL: http://dx.doi.org/10.1080/08927020701310915

Molecular Simulation, Vol. 33, Nos. 9–10, 15–30 August 2007, 733–745

Taylor & Francis
Taylor & Francis Group

A lattice kinetic Monte Carlo study of void morphological evolution during silicon crystal growth

J. DAI, W. D. SEIDER and T. SINNO*

Department of Chemical and Biomolecular Engineering, University of Pennsylvania, Philadelphia, PA 19104, USA

(Received December 2006; in final form March 2007)

A recently developed lattice kinetic Monte Carlo (LKMC) model for vacancy aggregation is used to investigate the morphological evolution of large vacancy aggregates under different conditions relevant to commercial silicon crystal growth. In particular, the roles of dissolved oxygen atoms as vacancy complexing agents during the aggregation process are studied and the resulting effects on the void morphological evolution are compared to recent experimental observations. It is shown that oxygen plays an important role, under certain crystal growth conditions, in the final morphology of vacancy clusters, and that the LKMC model is able to explain and accurately reproduce experimental observations. The essential dynamical features of the LKMC predictions are analyzed using a simple differential equation model to describe void growth kinetics under different conditions.

Keywords: Lattice kinetic Monte Carlo; Silicon; Vacancy aggregation; Oxygen; Oxygen–vacancy complexes

1. Introduction

The lattice kinetic Monte Carlo method (LKMC) has found applications in a large number of areas in which microscopic dynamical processes are important and an explicit representation of atomic-scale structure is required. The diffusion, reaction and aggregation of atomic species in crystals, such as point defects and impurity atoms, is a particularly suitable application that has been treated with LKMC in numerous studies. Recent examples of LKMC simulations applied to atomic diffusion and clustering in metallic and semiconductor systems are given in Refs. [1–5].

Recently, a LKMC model for vacancy aggregation was presented and used to analyze vacancy clustering in silicon [6,7]. Vacancy aggregation in crystalline silicon continues to plague polished wafers because nanoscale voids are harmful to microelectronic device performance measures, such as Gate-Oxide Integrity in DRAM circuits [8]. In these LKMC studies, careful attention was placed on the analysis of the lattice constraint in LKMC models, which greatly reduces the number of configurational degrees-of-freedom available to the system. It was shown that in real systems at elevated temperature, which is a common operating condition in semiconductor crystal growth and processing, most defects and clusters exist in configurations that are not aligned with the lattice. For example, vacancy clusters are not simply missing lattice atoms, but rather involve complex and substantial atomic relaxations that can extend several lattice parameters away from the actual vacant sites [9,10]. The configurational entropy associated with the ensemble of many distinguishable relaxations of each cluster therefore can be substantial and serves to significantly lower the free energy of vacancy aggregates as the temperature increases [11].

The importance of off-lattice degrees-of-freedom in a LKMC simulation makes the estimation of individual transition rates difficult if not impossible because the lattice structures allowed in the LKMC simulation are only idealizations of the actual structures. Moreover, each lattice structure corresponds to many potential continuous-space structures, which implies that each given transition between lattice structures corresponds to some average of transitions between the corresponding ensembles of actual structures. In order to address the underlying continuous-space degrees-of-freedom while retaining the computational advantages of the LKMC approach, a model-to-model regression approach was developed in Refs. [6,7], in which the LKMC transition rates were regressed by comparing the output of LKMC and

*Corresponding author. Email: talid@seas.upenn.edu

Molecular Simulation
ISSN 0892-7022 print/ISSN 1029-0435 online © 2007 Taylor & Francis
http://www.tandf.co.uk/journals
DOI: 10.1080/08927020701310915

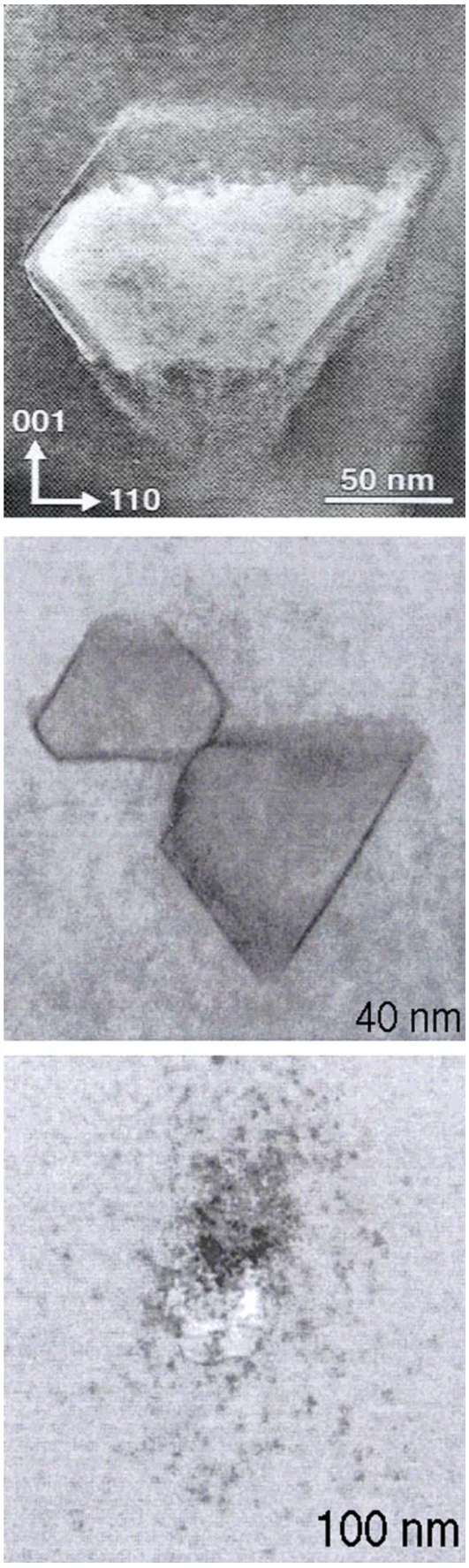

molecular dynamics (MD) simulations. Various measures were used in the model regression to ensure that the LKMC parameters were robustly specified, including transient cluster size distributions, large cluster density profiles, and cluster structural information.

In this paper, we extend and apply the LKMC model developed in Refs. [6,7] to the study of vacancy cluster morphology in the presence of a secondary species, namely oxygen. Oxygen, which is present in the crystal predominantly as single interstitial atoms, is an important element in commercial Czochralski (CZ) silicon crystals and plays the dual roles of impurity and dopant. Oxide precipitation during CZ crystal growth and wafer annealing serves to create essential gettering, or trapping, centers for harmful and highly mobile metal atoms introduced during device fabrication [12]. Oxide precipitates also provide mechanical toughness at elevated temperatures, which is particularly important for large-diameter wafers. On the other hand, the presence of oxide precipitates in the near-surface region of a wafer where the devices are fabricated is highly undesirable.

The presence of a large oxygen concentration, which is typically about 10^{17}–$10^{18}\,\mathrm{cm}^{-3}$ and several orders-of-magnitude larger than the vacancy concentration, can strongly influence the vacancy aggregation process and resulting void morphology [13–15]. Under typical CZ growth conditions, vacancy aggregation proceeds in a rather narrow temperature interval between 1100 and 1070°C [16–18]. The basic mechanism for void formation is well understood. Vacancies and self-interstitials are introduced into the crystal at the melt–solid interface at their respective equilibrium concentrations and then proceed to recombine as the cooling crystal lowers the equilibrium concentrations and creates point defect supersaturation. Above a critical pulling velocity, vacancies, which possess the larger equilibrium concentration, eventually deplete all of the self-interstitials and become increasingly supersaturated across most of the crystal driving homogeneous nucleation of voids [19,20]. The final void size distribution depends on the post-recombination vacancy concentration and the crystal cooling rate during void formation—higher cooling rates produce a larger number of smaller voids [16,18].

If the oxygen concentration is low, vacancy aggregation proceeds essentially without being affected by the presence of oxygen because the oxygen solid solution does not become sufficiently supersaturated before most of the vacancy aggregation is completed. Under these conditions, large single octahedral voids (figure 1(a)) are formed with mean diameter of about 100 nm [13,14,21,22]. As the crystal continues to cool, the interstitial oxygen atoms diffuse to and segregate on the void internal surface and produce an oxide coating several nanometers thick.

Figure 1. TEM images of various void structures observed in CZ and oxygen-doped FZ crystals. (a) Single octahedral void (CZ crystal), (b) double void (CZ crystal), (c) void cloud (oxygen doped FZ crystal). Taken from Refs. [13,14,21].

Higher interstitial oxygen concentrations are associated with the formation of double and triple void structures (figure 1(b)) [13,14]. Previous qualitative models have postulated that double and triple void structures arise due to simultaneous vacancy aggregation and oxide deposition on the still-evolving voids [12,23,24]. As a vacancy aggregate is still growing, the surface becomes partially covered with oxide, which then leads to the formation of heterogeneous growth sites from which secondary voids grow. Finally, oxygen doped floating-zone (OFZ) crystals [14], which are subject to very high cooling rates (several times higher than CZ), have been shown to lead to very different void structures when the oxygen concentration is about $8 \times 10^{17}\,\mathrm{cm}^{-3}$ (similar to moderately high oxygen concentration CZ crystals). In the OFZ crystals, voids are observed to have a compound structure in which a central void (with diameter ~ 50 nm) is surrounded by a cloud of secondary nanoscopic voids (figure 1(c)). The secondary void cloud consists of 2–3 nm diameter voids distributed over a 100 nm spherical region centered about the primary void. The formation mechanism of the void cloud structure is not yet firmly elucidated. The aim of this paper is to explain the formation mechanisms of these various void structures using direct LKMC simulations.

The remainder of the paper is organized as follows. In the following section, LKMC models are presented for vacancy aggregation and oxygen–vacancy interactions. In Section 3, the formation mechanisms of the double/triple void (figure 1(b)) and void cloud structure (figure 1(c)) are discussed in detail. Finally, conclusions are presented in Section 4.

2. Vacancy–vacancy and oxygen–vacancy interaction models

2.1 Vacancy–vacancy interactions

An interaction model for vacancies has already been addressed in previous work [6,7] and is only discussed briefly here. Vacancies are assumed to interact up to the 8th nearest-neighbor (NN) shell based on MD simulation results [9,10] using the empirical EDIP potential [25]. A "vacancy–vacancy bonding energy", E_b^j, is defined at each interaction distance so that the energy barrier for a vacancy hop is given by Ref. [6]

$$\Delta E_i = \max\left(0, \Delta E_{\mathrm{hop}} - 0.5 \times \sum_{j=1}^{\mathrm{NN}} \Delta \mathrm{NB}_j E_b^j\right), \quad (1)$$

where ΔE_i is the energy barrier for event i, where ΔE_{hop} is the energy barrier for a single, isolated vacancy jump, NN is the maximum interaction shell, $\Delta \mathrm{NB}_j$ is the bond count change due to a hop associated with interaction range j. Note that the barrier function in equation (1) is positive semi-definite, i.e. no negative barriers are possible. The rate of an event i is then simply given by an Arrhenius expression of the form

$$r_i = v_0 \exp\left(\frac{-\Delta E_i}{k_B T}\right), \quad (2)$$

where r_i is the rate for event i, v_0 is a (constant) attempt frequency, k_B is the Boltzmann constant and T is the simulation temperature.

The eight bonding energies, $\{E_b^j, j = 1{,}8\}$ are derived by regression to MD data of various types including those generated by large-scale simulations of aggregation, single cluster structures and density profiles, and cluster diffusivities [6]. Collectively, these eight bond energies define a "lattice potential" for the LKMC model. As mentioned earlier in the Introduction, an important feature of the derived lattice potential is that it accounts implicitly for the missing configurational degrees of freedom associated with the underlying real, continuous-space lattice. It should be noted that the magnitude of the implicit continuous-space configurational entropy is strongly temperature dependent and therefore the regressed effective vacancy–vacancy bond energies also are functions of temperature. The model in refs. [6,7] and all results presented in this work were obtained at a single temperature of 1600 K.

A screening model was introduced into the LKMC physics in Refs. [6,7] to account for the fact that void formation energies in a solid are defined by the void surface area, and not the volume. In this model, vacancies only interact with each other if the path connecting them is not obstructed by other vacancies [6]. It was demonstrated that this physical feature leads to much better agreement with MD results than could otherwise be achieved. However, the presence of interaction screening effectively renders the lattice potential a many-body one, and significantly increases its computational expense.

2.2 Vacancy–oxygen complex formation

There is extensive evidence for the formation of various oxygen–vacancy complexes in bulk CZ silicon but their exact nature is still under some debate [24,26–28]. The OV and O_2V complexes are commonly accepted to be the dominant mediators for trapping vacancies and form according to the reaction

$$\mathrm{V} + \mathrm{O} \leftrightarrow \mathrm{OV} + \mathrm{O} \leftrightarrow \mathrm{O_2V}. \quad (3)$$

The OV complex is considered to be less stable than the O_2V complex, and should exist in much lower concentrations [28]. The diffusivity of interstitial oxygen is several orders-of-magnitude slower than that of the single vacancy at all temperatures [29] but the diffusion coefficients of the oxygen–vacancy complexes are not well established, although they are not expected to be larger than the single interstitial oxygen value.

As will be shown in Section 3, the exact nature of the oxygen–vacancy binding mechanism is not important for assessing the influence of bulk vacancy trapping on the evolution of void morphology. The oxygen–vacancy binding physics in the present LKMC model are represented

schematically by the following single process:

$$\mathrm{V} + {}^{*} \leftrightarrow \mathrm{V}^{*}, \tag{4}$$

where $*$ represents a lattice site occupied by an oxygen atom which binds to the vacancy to create a trapped-vacancy complex, $V*$. Two mechanistic models for this process are considered. In the first model (Model 1 shown in figure 2), the oxygen atom, or trapping site, is immobile but the vacancy can reversibly bind and unbind from it. The unbinding rate is given by λr, where r is the normal rate of vacancy hopping (for a given surrounding environment) and λ is a trapping strength factor which represents the reduced mobility of the vacancy once it complexes with an oxygen atom. Once the vacancy moves away from the trapping site it resumes a normal hopping rate. In the second model that we consider (Model 2 shown in figure 3), the vacancy binds irreversibly with the trapping site and diffuses with the oxygen atom at a reduced rate also given by λr. In both models, the sites adjacent to a trapped vacancy are also designated as trapping sites, which reflects the finite capture radius of an oxygen–vacancy complex. Both models are considered in a parametric study in the following section.

2.3 *Oxide formation on void surfaces*

The reversible formation of oxygen–vacancy complexes can be characterized by an equilibrium constant of the form, $K_{\mathrm{V}^*} = [\mathrm{V}^*]/[\mathrm{V}][^*]$, where $*$ denotes the oxygen trapping sites. As a result, the extent of vacancy complex formation depends on both the concentrations of free vacancies and interstitial oxygen. In particular, if the vacancy concentration is only weakly supersaturated (or not at all) because of ongoing vacancy aggregation, the formation of oxygen–vacancy complexes may be negligible even if the single interstitial oxygen atoms are supersaturated. On the other hand, the formation of oxide on the surfaces of voids only requires an oxygen supersaturation and is independent of the free vacancy concentration. As a result, under certain growth conditions, such as high oxygen levels and moderate cooling rates, it is possible to have a driving force for oxide layer formation without any bulk oxygen–vacancy complex formation.

In this work, the effect of oxide layer formation on the void morphological evolution is investigated with a simple model. Oxygen atoms are assumed to arrive spontaneously at a void surface at a rate that is determined by diffusion limited dynamics. Once an oxygen atom is incorporated at a surface vacancy site, that site becomes an "oxide site". An oxide site differs from a vacancy site in the following ways:

(1) Oxide mobility on the void surface is reduced by a factor λ relative to vacancy mobility.
(2) Free vacancies do not interact with oxide particles (see further explanation below).
(3) Oxide–oxide interactions are the same as vacancy–vacancy interactions.

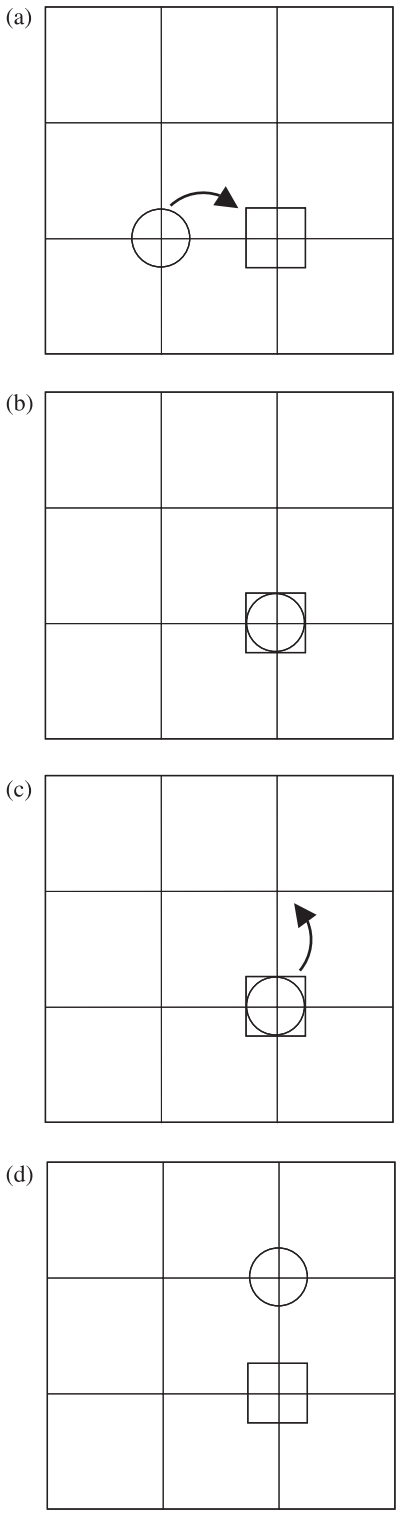

Figure 2. Model 1—Reversible binding and immobile trapping sites. (a) Vacancy binding, (b) bound OV complex, (c) dissociation, and (d) free vacancy. Circle, free vacancy; square, interstitial oxygen; circle-in-square, OV complex.

(4) Physically, oxide particles cannot be entirely surrounded by vacancies—they must either be connected to other oxide particles or to the silicon lattice. This is ensured in the simulation by exchanging oxide particle positions with an arriving vacancy if all other NNs are vacancies.

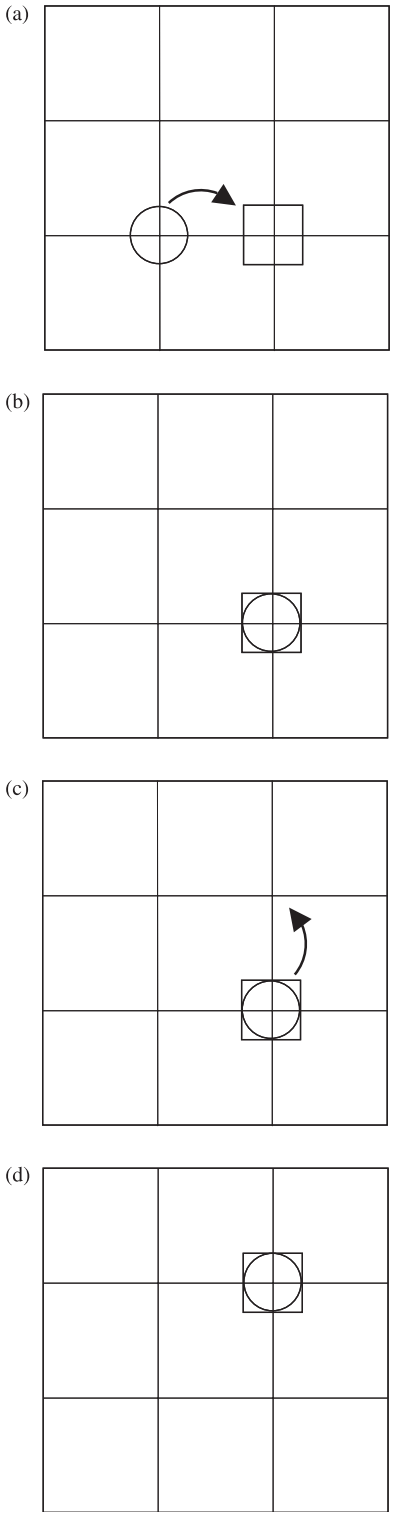

Figure 3. Model 2—Irreversible binding and mobile trapping sites. (a) Vacancy binding, (b) bound OV complex, (c) complex diffusion, and (d) irreversible complex. Circle, free vacancy; square, interstitial oxygen; circle-in-square, OV complex.

Assumption 2 above requires further explanation. In Section 2.2, it was assumed that interstitial oxygen atoms (in the form of isolated trapping sites) and vacancies interacted in the same way that vacancies interacted with other vacancies — only the mobility of the resulting oxygen–vacancy complex was modified. Within assumption 2, however, the interaction between incoming vacancies and oxide deposited on a void surface is assumed to be very weak. The difference in the two models of oxygen–vacancy interaction is motivated by the very different stress environments experienced by oxide particles formed in the lattice bulk and oxide deposited on void surfaces. Interstitial oxygen atoms and oxide precipitates in the lattice bulk are associated with large compressive stresses that attract vacancies [30,31]. On the other hand, the stress associated with oxide formed on a void surface is passivated (relieved) by the presence of the void, i.e. the oxide can expand into the void volume as required to minimize the stress energy.

3. Results and discussion

Formation mechanisms for the void morphologies shown in figure 1(b),(c) are addressed separately below. The formation of cloud-like structures (figure 1(c)) is considered first in Section 3.1, while the formation of multiple-primary void structures (figure 1(b)) is addressed in Section 3.2.

3.1 Vacancy–oxygen complex formation and cloud-like void morphology

It has been suggested that the cloud-like void structure shown in figure 1(c) forms because of a sudden shift of the $V + O \rightarrow OV + O \rightarrow O_2V$ reactions to the right before the vacancy aggregation process is complete. The rapid cooling rate encountered in OFZ crystallization (about ten times higher than that in standard CZ [14]) produces an oxygen supersaturation quickly relative to the vacancy aggregation (diffusion limited) timescale and couples the oxygen–vacancy binding and vacancy aggregation processes. In this picture, the resulting cloud of secondary voids therefore is an instantaneous snapshot of the (trapped) vacancy profile surrounding the growing primary void.

Consider, however, that the vacancy distribution profile around a void under typical void growth conditions would be at least partially established by diffusion limitations [32]. For fully diffusion-limited growth, the concentration of vacancies at the cluster surface would approach the local equilibrium value, while far away from the growing void the concentration would tend towards the bulk value, as shown schematically in figure 4.

On the other hand, an important feature of the secondary void cloud shown in figure 1(c) is that the cloud density *increases* towards the primary void, i.e. a diffusion-limited vacancy concentration profile is inconsistent with the idea that the void growth is interrupted by sudden vacancy binding into immobile complexes which then serve as nucleation sites for new clusters.

LKMC simulations based on the model described in Section 2.1 were used to investigate possible mechanisms

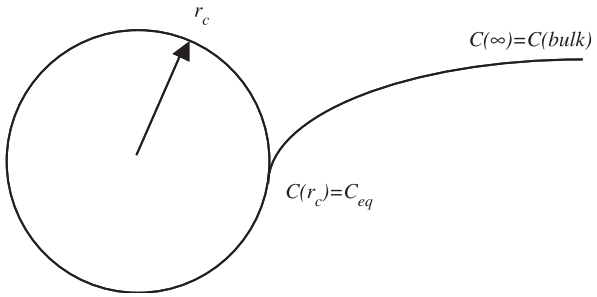

Figure 4. Quasi-steady state single vacancy profile in the vicinity of void under diffusion-limited growth conditions.

for the formation of void clouds using the following simulation conditions. An octahedral void containing 16,215 vacancies initially was placed in a lattice containing 5.83×10^6 sites and subject to periodic boundary conditions. The system was then allowed to evolve without constraint at a fixed temperature of 1600 K. A control run first was performed in which no oxygen traps were present. In this case, the void emits approximately 35–40 monomer vacancies, but otherwise retains its octahedral geometry and establishes equilibrium with the surrounding lattice as shown in figure 5. The void is stable at 1600 K because the system is closed. The void size is plotted as a function of time in figure 6 and shows clearly the dynamical equilibrium that has been established in the system.

The effective single vacancy concentration in equilibrium with the void is about $3.4 \times 10^{17}\,\mathrm{cm}^{-3}$, which is substantially higher than the value, $7.6 \times 10^{14}\,\mathrm{cm}^{-3}$, predicted by the EDIP potential at 1600 K [9]. Recall that the EDIP potential was used to generate all of the MD data to which the LKMC bond energies were regressed. The high equilibrium vacancy concentration arises because of the Gibbs–Thomson effect [33], whereby the void exerts a local thermodynamic pressure on the lattice leading to higher vacancy solubility in the vicinity of the void.

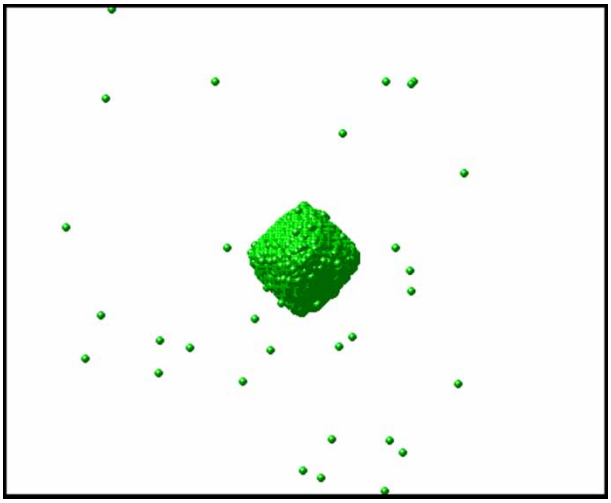

Figure 5. Snapshot of a pre-seeded 16,215-vacancy void after 5 μs of annealing at 1600 K.

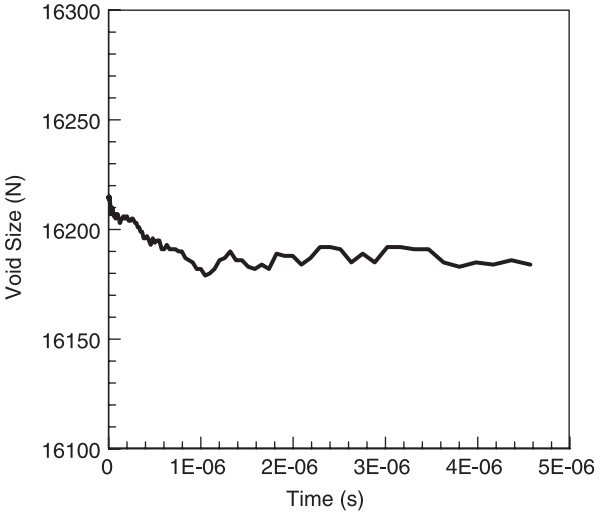

Figure 6. Primary void size as a function of time predicted by LKMC simulation at 1600 K. Initial void size = 16,215. No oxygen traps.

The presence of oxygen traps dramatically changes the system behavior. In figure 7, the primary void size is shown to decrease rapidly in time when oxygen traps are introduced randomly into the system at about 1% atomic fraction (assuming Model 1 binding physics—see Section 2.B). Three different trap strengths were used; $\lambda = 10^{-2}$, $\lambda = 10^{-4}$ and $\lambda = 10^{-6}$, where λ approximately represents the ratio of trapped-to-free vacancy diffusivities. Literature values for the oxygen and vacancy diffusion coefficients at 1100°C, the temperature at which void aggregation typically proceeds during CZ crystal growth, give $D_O/D_V \sim 5 \times 10^{-5}$ [29]. Assuming that $D_{OV} \sim D_{O_2V} \sim D_O$, λ can be considered to be roughly equivalent in meaning to the ratio D_O/D_V. The rate of primary void size decrease increases strongly with the trapping strength, λ, while for $\lambda = 10^{-2}$ the system is essentially unchanged relative to the control case.

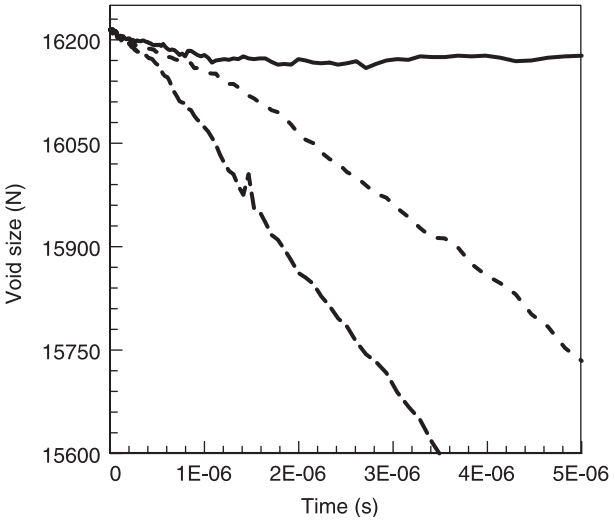

Figure 7. Primary void size as a function of time predicted by LKMC simulation at 1600 K. Initial void size = 16,215 with 1% oxygen traps dispersed randomly in the lattice (Model 1). Solid line–$\lambda = 10^{-2}$, dashed-line–$\lambda = 10^{-4}$, long-dashed line $\lambda = 10^{-6}$.

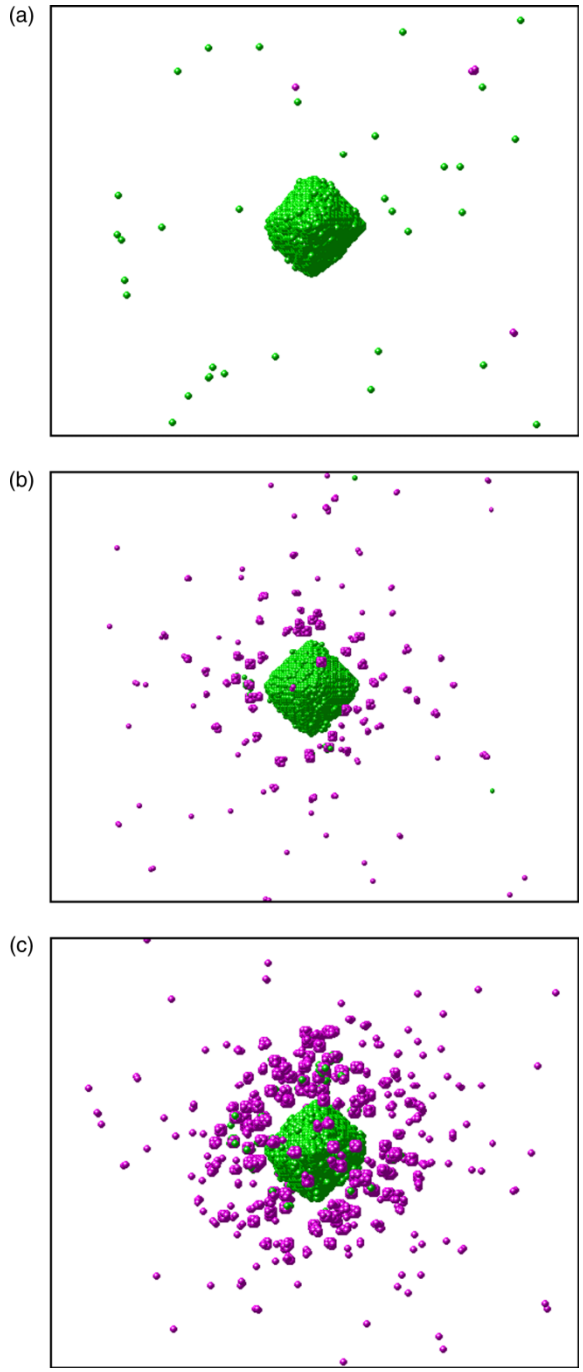

Figure 8. Snapshots of vacancy positions after 6 μs with trap concentration = 1.0%. Green spheres represent free vacancies, purple spheres represent trapped (complexed) vacancies. (a) $\lambda = 10^{-2}$, (b) $\lambda = 10^{-4}$ and (c) $\lambda = 10^{-6}$ (Colour in online version).

Shown in figure 8 are snapshots of the system after 6 μs for various trapping strengths. For the $\lambda = 10^{-4}$ and $\lambda = 10^{-6}$ cases, the formation of a secondary cloud-like distribution of small vacancy clusters (purple atoms) can be seen clearly. These clusters are formed by the *dissociation* of the primary void once the traps are activated. A mechanism for the formation of the secondary-void cloud therefore can be proposed on the basis of the results presented above: During rapid cooling in OFZ crystals the vacancy aggregation process is interrupted by the onset of oxygen–vacancy binding (i.e. equation (4) shifts to the right) because of the rising oxygen supersaturation. The remaining free vacancies in the crystal bulk are now bound into slow-diffusing (or even immobile) oxygen complexes. As a result, voids that have already been formed lose stability and begin to dissociate to replenish the free vacancy population back to its equilibrium value. In other words, the osmotic pressure exerted by the vacancy solid-solution on the existing voids is effectively removed if the free vacancies are *sufficiently* immobilized in the lattice. It is interesting to note that substantial immobilization is required to produce this effect—for the $\lambda = 10^{-2}$ case (corresponding to $D_{V^*}/D_V = 0.01$), almost no vacancy emission is observed relative to the control case in the simulation time considered.

Finally, the emitted vacancies diffuse away from the primary void and get captured by the surrounding oxygen atoms, gradually building up a distribution of small secondary vacancy clusters around the primary void. Note that the secondary clusters are vacancy aggregates; essentially only a single oxygen atom is needed to provide the nucleation site. This is in agreement with the experimental observation (via Energy Dispersive X-Ray Spectroscopy (EDS) analysis) that the secondary clusters do not contain oxide [14].

The exact distribution of the secondary void cloud depends on the primary void size, the concentration of oxygen traps, and the capture radius and mobility of the oxygen–vacancy complexes. However, the overall qualitative behavior is unchanged for reasonable values of these parameters. Shown in figure 9 are snapshots of the vacancy distribution at 5 μs for several different trapping-site concentrations. While the cloud density and localization increase with increasing oxygen concentration, the overall morphology is qualitatively unaffected.

The results also are robust with respect to the assumed binding physics. Shown in figure 10 are snapshots of the vacancy distribution after 5 μs using Model 2 (Section 2.1) to represent the oxygen–vacancy binding physics. For strong binding, $\lambda = 10^{-6}$, the primary void begins to dissociate once traps in the lattice start immobilizing the vacancy solid-solution in equilibrium with the void as in the previous cases (figure 10(b)). However, Model 2 predicts qualitatively different behavior when the mobility of the trapped vacancy is increased. In the $\lambda = 10^{-2}$ case, the trapped vacancies now remain sufficiently mobile to continue diffusing and interact directly with the cluster. As the cluster surface becomes heterogeneously mobile because of the presence of oxide, it becomes distorted and the cluster shape evolution changes. Void shape evolution in the presence of oxygen is addressed further in the following section.

A final note should be made regarding the 1600 K temperature employed in all the LKMC simulations described in this section, as well as the ones in the following sections. As discussed in the Introduction, vacancy

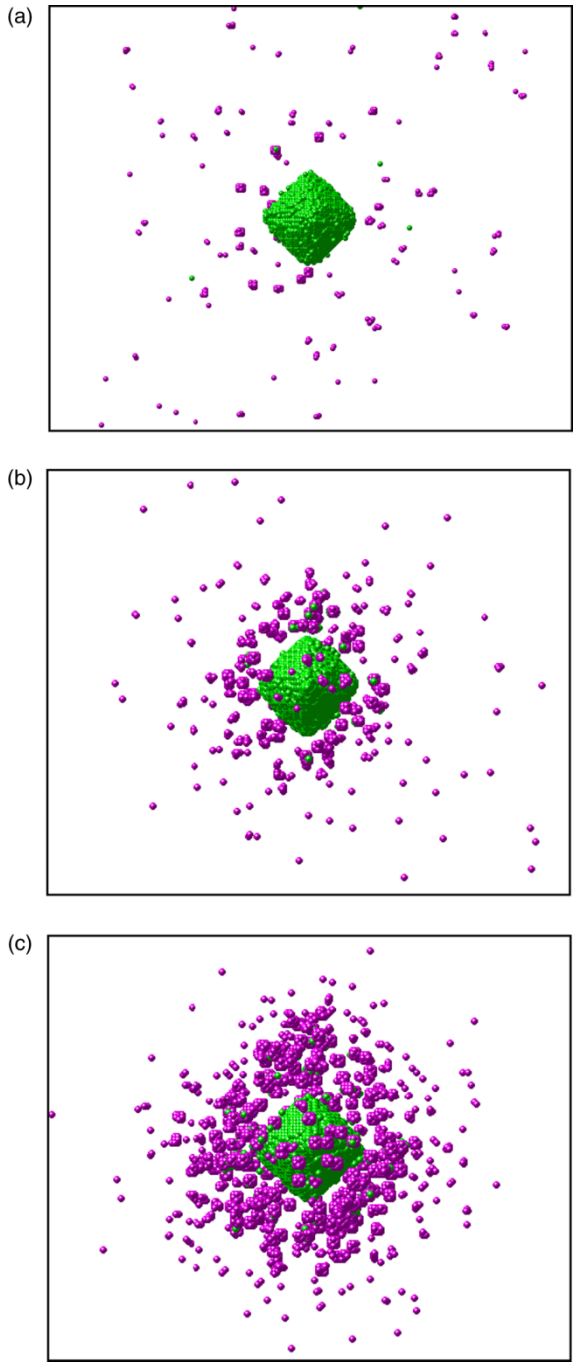

Figure 9. Snapshots of vacancy positions after 5 μs as predicted by Model 1 with $\lambda = 10^{-6}$. Green spheres represent free vacancies, purple sphere represent trapped (complexed) vacancies. Trap concentrations are (a) 0.1%, (b) 1%, and (c) 5% (Colour in online version).

aggregation during CZ crystal growth takes place in the neighborhood of 1100°C (or 1373 K), and at somewhat lower temperatures in FZ and OFZ crystals. The fact that our simulations were performed at a single temperature of 1600 K affects the results and conclusions quantitatively, but not qualitatively. For example, the timescales for void dissolution and the equilibrium free vacancy concentration will depend on temperature, but the overall process will be unaffected.

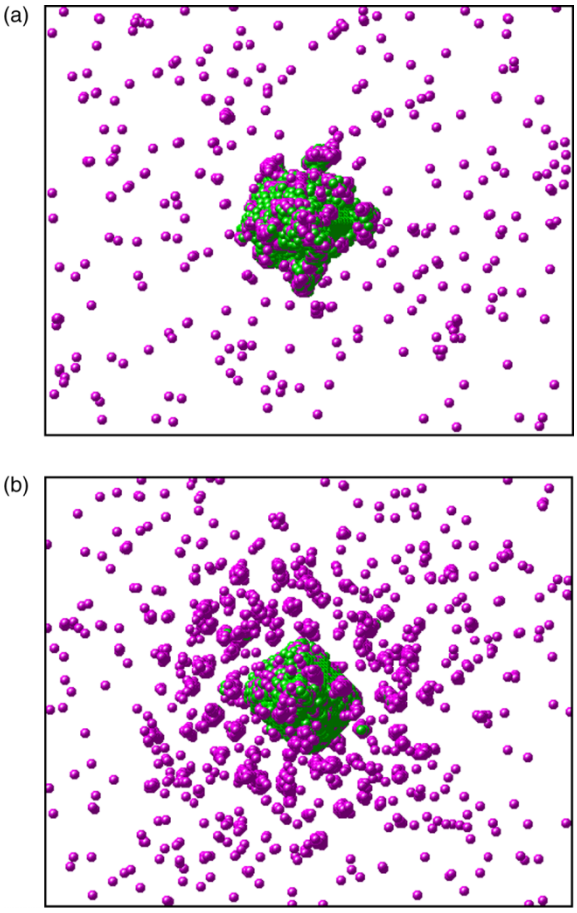

Figure 10. Snapshots of vacancy positions after 5 μs as predicted by Model 2 with trap density = 1.0%. Green spheres represent free vacancies, purple sphere represent trapped (complexed) vacancies. Mobility ratios are (a) $\lambda = 10^{-2}$, (b) $\lambda = 10^{-6}$ (Colour in online version).

3.2 Oxide-layer deposition and double/triple void morphology

LKMC simulations performed with different trap densities and mobilities indicate that the dissolution mechanism described in the previous section is not likely to also explain the evolution of the double and triple void morphology found in CZ crystals with high oxygen concentration. Briefly, too much time would be needed to transfer enough vacancies from the primary void to a second void that is almost equal in size. Moreover, there is no clear driving force that would cause the vacancies emitted from the primary void to travel preferentially in one direction to create a single additional void.

Previous models [23,24] have addressed the formation of double and triple voids in the context of a *growth* mechanism, whereby the void shape evolution is distorted by the simultaneous deposition of oxide on the void surface. The lower cooling rates found in CZ growth, relative to OFZ, suggests the following qualitative picture: Sometime after point defect recombination is completed, and vacancy aggregation begins at about 1100°C, the oxygen solid-solution becomes supersaturated. The relatively slow cooling rate allows vacancy aggregation

to proceed to an extent that keeps the vacancy concentration close to its equilibrium value and the oxygen–vacancy binding reactions in equations (4) are not substantially activated as was the case in the fast-cooled OFZ crystal. However, the driving force for oxide precipitation on void surfaces is present, and if the oxygen concentration is high enough, oxide precipitation on void surfaces will take place concurrently with void growth.

In this section, we employ two modeling approaches to study the influence of oxide layer formation on void shape evolution during growth. First we use LKMC simulations based on the model described in Section 2 to explicitly probe cluster morphology, and then we develop a mean-field model to analyze quantitatively the LKMC predictions.

3.2.1 LKMC simulations of void growth in the presence of oxide layer formation. LKMC simulations were performed to assess the impact of an insulating surface oxide coating on the growth behavior of pre-seeded octahedral voids. As mentioned earlier, the present LKMC model is valid only at a single temperature (1600 K) and therefore the driving force for void growth must be supplied by creating a vacancy supersaturation, rather than by crystal cooling. This was achieved by imposing a monomer controller on a system containing a pre-seeded octahedral void whereby the number of single vacancies in the lattice is fixed so that a constant supersaturation is created. The controller monitors periodically the single vacancy number and either adds or removes vacancies to drive the system towards the set-point. It was found that large supersaturations led to the formation of secondary clusters which competed for monomers and inhibited the growth of the pre-seeded void, while small monomer set-points (corresponding to an undersaturation) led to void dissolution, as expected. Intermediate supersaturations of about 2–4 led to the fastest seed growth. The following LKMC simulations were all performed starting with a single pre-seeded octahedral void containing 6545 vacancies in a 1.73×10^6-site lattice. The optimal monomer set-point number in this system size was determined to be 89, which corresponds to a supersaturation of approximately 3.

Several LKMC runs were performed in which the void surface oxidation rate and the initial oxide coverage were varied. Shown in figure 11 are three snapshots taken from LKMC simulations with different oxide deposition schedules. Slow deposition rates (figure 11(a)) essentially do not modify the growth behavior relative to the oxide-free case because the amount of void surface available for vacancy attachment increases faster than the rate of passivation by oxide coverage. At very high oxide deposition rates (figure 11(b)), the void growth process ceases quickly because the entire surface becomes completely passivated and the void no longer provides a favorable sink for single vacancies. More interesting behavior is observed at intermediate oxide deposition rates as shown in figure 11(c). In this case, a double void structure is clearly seen to evolve, supporting the hypothesis that the coupling between oxide deposition and void growth is responsible for the formation of double and triple void structures.

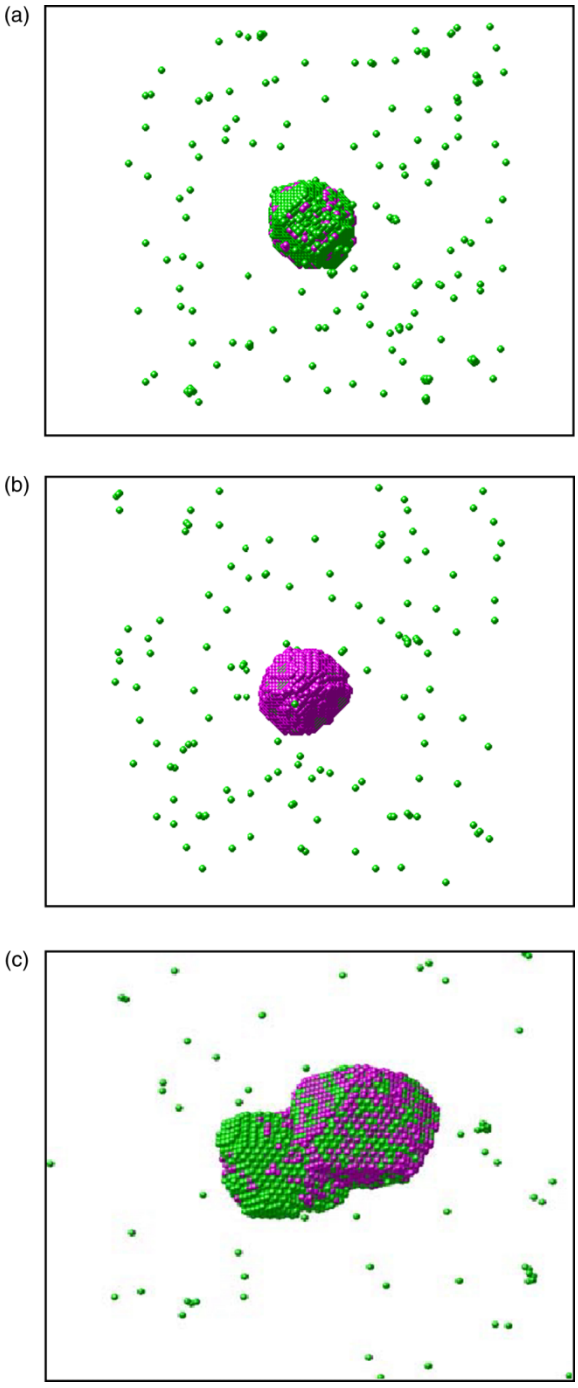

Figure 11. Snapshots of void structures grown under constant monomer supersaturation (approx. 3) for different surface oxide deposition rates. Green spheres represent free vacancies, purple spheres represent surface oxide. (a) Low oxide deposition rate, (b) high oxide deposition rate, and (c) intermediate oxide deposition rate (Colour in online version).

The void evolution dynamics leading to the structures shown in figure 11 are analyzed further in the following section using a mean-field model.

3.2.2 A mean-field model for void growth with oxide layer formation. A mean-field dynamic model was developed to analyze quantitatively the results presented in the previous section. Consider a growing void containing $N(t)$ vacancies. The growth rate of the void is given by the product of the flux of vacancies at the void surface, J, and the active void surface area, A_{eff}, so that

$$\frac{\mathrm{d}N}{\mathrm{d}t} = J{\cdot}A_{\text{eff}} = J{\cdot}(A - A_{\text{o}}). \tag{5}$$

In equation (5), A is the total void surface area, and A_{o} is the void surface area covered by passivated oxide, which does not interact with incoming vacancies. Assuming spherical geometry, the total void surface area is given by

$$A = (4\pi)^{1/3}(3V_1)^{2/3}N^{2/3}, \tag{6}$$

where V_1 is the volume of a single vacancy. Further assuming that all the oxide particles are located on the void surface, the coated area is given by

$$A_{\text{o}} = (4\pi)^{1/3}(3V_1)^{2/3}\frac{N_{\text{o}}}{3}. \tag{7}$$

For a constant rate of oxygen atom arrival at the void surface, k, the growth rate of a void can be obtained by combining equations (5)–(7) to give

$$\frac{\mathrm{d}N}{\mathrm{d}t} = J{\cdot}(4\pi)^{1/3}(3V_1)^{2/3}\left[N^{2/3} - \frac{N_{\text{o}}}{3}\right], \tag{8}$$

and

$$\frac{\mathrm{d}N_{\text{o}}}{\mathrm{d}t} = k. \tag{9}$$

A model for the vacancy arrival flux, J, can be proposed based on the theory of Lifshitz and Slyozov [33]. Consider the steady-state spherical diffusion-limited problem

$$\frac{1}{r^2}\frac{\partial}{\partial r}\left(r^2 D_1 \frac{\partial C}{\partial r}\right) = 0, \tag{10}$$

where r is the radial coordinate emanating from the center of a spherical void, C is the concentration of vacancies surrounding the void and D_1 is the single vacancy diffusivity (figure 4). Equation (10) is subject to the boundary conditions that the far-field vacancy concentration equals some set-point value, $C(\infty) = C^{\text{sp}}$, and the concentration at the surface of the growing void is $C(r_c) = C^{\text{eq}}$ where C^{eq} is the equilibrium concentration of vacancies at the surface of the void ($r = r_c$). The solution of equation (10) with these boundary conditions gives

$$C = (C^{\text{SP}} - C^{\text{eq}})\left(1 - \frac{r_c}{r}\right) + C^{\text{eq}}. \tag{11}$$

The vacancy flux at the surface, therefore, is

$$J = D_1\left(\frac{\partial C}{\partial r}\right)_{r=r_c} = \frac{D_1(C^{\text{SP}} - C^{\text{eq}})}{r_c}. \tag{12}$$

Expressing the radius of the cluster in terms of the vacancy number and volume, $r_c = ((3NV_1)/(4\pi))^{1/3}$, and applying equation (12) to equation (8) the void growth rate is given by

$$\frac{\mathrm{d}N}{\mathrm{d}t} = (4\pi)^{2/3}(3V_1)^{1/3}D_1(C^{\text{SP}} - C^{\text{eq}}) \times \left[N^{1/3} - \frac{N_{\text{o}}}{3N^{1/3}}\right]. \tag{13}$$

Defining $\beta = (4\pi)^{2/3}(3V_1)^{1/3}D_1[C^{\text{SP}} - C^{\text{eq}}]$, equation (13) can be rewritten in final form as

$$\frac{\mathrm{d}N}{\mathrm{d}t} = \beta\left[N^{1/3} - \frac{N_{\text{o}}}{3N^{1/3}}\right]. \tag{14}$$

To compute the void growth rate, equation (14) must be solved together with equation (9) with appropriate initial conditions for N and N_0.

3.2.3 Self-consistent comparison of mean-field and LKMC models. Comparisons between the mean-field and LKMC predictions for void size evolution were made for several operating conditions. First, void size evolution in the absence of oxygen was considered ($k = 0$), where the mean-field growth kinetics simplify to

$$\frac{\mathrm{d}N}{\mathrm{d}t} = \beta N^{1/3}. \tag{15}$$

Equation (15) was solved analytically with the initial condition, $N(t = 0) = 6545$ and with $C^{\text{SP}} = 89$, corresponding identically to the values used in the LKMC simulations described in the previous section. The value for C^{eq} (and therefore β) is difficult to estimate independently from LKMC simulation and was obtained by regressing the analytical solution to the LKMC. The difficulty stems from the expected non-uniform effect of the Gibbs–Thomson phenomenon on the equilibrium vacancy distribution around a void. Attempts to compute independently the single vacancy concentration in equilibrium with a void of size 6545, led to $C^{\text{eq}} \sim 30$, which is a factor of two lower than the regressed value of $C^{\text{eq}} = 60$ (which corresponds to $\beta \sim 3 \times 10^6\,\text{s}^{-1}$). It is entirely possible that the effective equilibrium concentration at the void surface is higher than the value averaged over the entire simulation cell but this value is impossible to evaluate accurately in such a small system.

The void size evolutions predicted by LKMC and the analytical model using $C^{\text{eq}} = 60$ ($\beta \sim 3 \times 10^6\,\text{s}^{-1}$) are shown in figure 12 and the agreement is excellent across the entire timescale simulated. The fact that the LKMC evolution follows the analytical result closely demonstrates that the diffusion-limited quasi-steady-state assumption is valid, i.e. there is essentially no reaction barrier for incorporating single vacancies into the growing void. Under these conditions the void grows at an increasing rate, and for the supersaturation considered here, the surface diffusion rate is sufficiently high to keep the void growing with compact morphology.

For high oxide deposition rate, however, the void active surface area is reduced as the void grows. Shown in figure 13

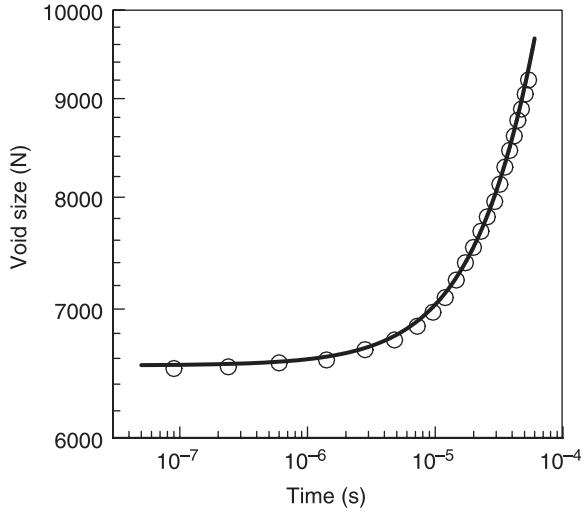

Figure 12. Comparison between mean-field and LKMC predictions for void size evolution without oxidization. Circles, LKMC; solid line, mean-field model.

are the predictions for the void size and surface oxide coverage fraction, θ, when the oxidization rate, k, is fixed at $4 \times 10^7\,s^{-1}$, but with the same initial conditions as in the previous case. Once again the agreement between the mean-field and LKMC models is excellent for both quantities. Initially the void grows as in the oxide-free case, but as the coverage increases the growth rate declines, and at about 2 μs, the void suddenly becomes fully passivated and stops growing. A dimensionless ratio of timescales for oxide and vacancy deposition rates can be defined as $\chi \equiv k/\beta$. For $k = 4 \times 10^7\,s^{-1}$, $\chi \sim$ O(10) which quantitatively shows that the overall growth rate is governed by the oxide deposition rate at these conditions.

The above situations correspond to the structures shown in figure 11(a),(b). The double void structure shown in figure 11(c) was obtained using a two-stage growth

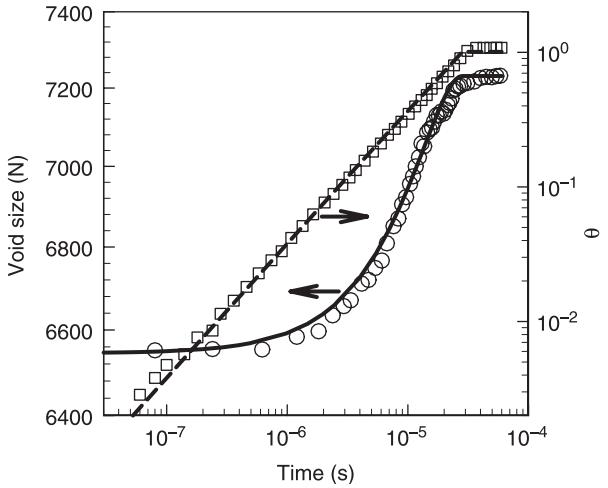

Figure 13. Comparison between mean-field and LKMC predictions for void size evolution with oxidization ($k = 4 \times 10^7\,s^{-1}$). Circles, void size from LKMC simulation; squares, surface coverage of oxide from LKMC simulation; solid line, void size from mean-field model; dashed line, surface coverage of oxide from mean-field model.

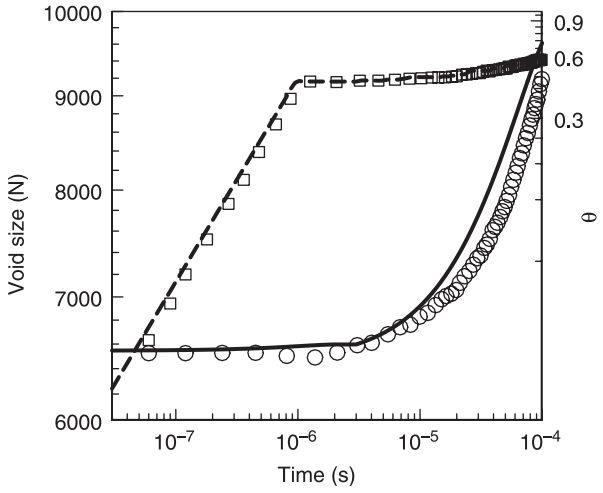

Figure 14. Comparison between mean-field and LKMC predictions for void size evolution with oxidization. Circles, void size from LKMC simulation; squares, surface coverage of oxide from LKMC simulation; solid line, void size from mean-field model; dashed line, surface coverage of oxide from mean-field model.

process. For $t < 2\,\mu s$, $k = 5 \times 10^8\,s^{-1}$, or $\chi \sim$ O(100), was used, while for $t > 2\,\mu s$, $k = 8.5 \times 10^6\,s^{-1}$, or $\chi \sim 3$, was applied. All other parameters were the same as in the previous two runs. The rapid surface oxidation rate for $t < 2\,\mu s$ was used to mimic the presence of a partial oxide layer which would be expected by the time the primary void grew to its initial simulation size (i.e. 6545 vacancies). The two-step procedure is practically identical to simply initiating the simulation with a partially-oxidized void, but avoids any bias in the placement of the oxide particles.

The mean-field and LKMC predictions for the void size and oxide coverage fraction for this two-stage process are shown in figure 14. The agreement between the two models is excellent at the initial stages where the surface oxidation rate is rapid relative to the void growth and gradually becomes worse as the double void morphology evolves. This small discrepancy is expected because the assumed values for the geometric factors in the mean-field model (i.e. based on spherical geometry) do not apply to the double void structure. The important point to note, however, is that the double void morphology evolves when $\chi \sim$ O(1), i.e. when the oxide and vacancy fluxes are similar during void growth.

4. Conclusions

A comprehensive analysis, based on direct LKMC simulations, was presented to explain the origin of the various void morphologies that are encountered in single silicon crystals grown by the CZ and FZ processes. It was demonstrated that properly parameterized LKMC models are powerful tools for probing the microstructure of mesoscopic defects that are commonly found in commercial semiconductor silicon crystals. Both the

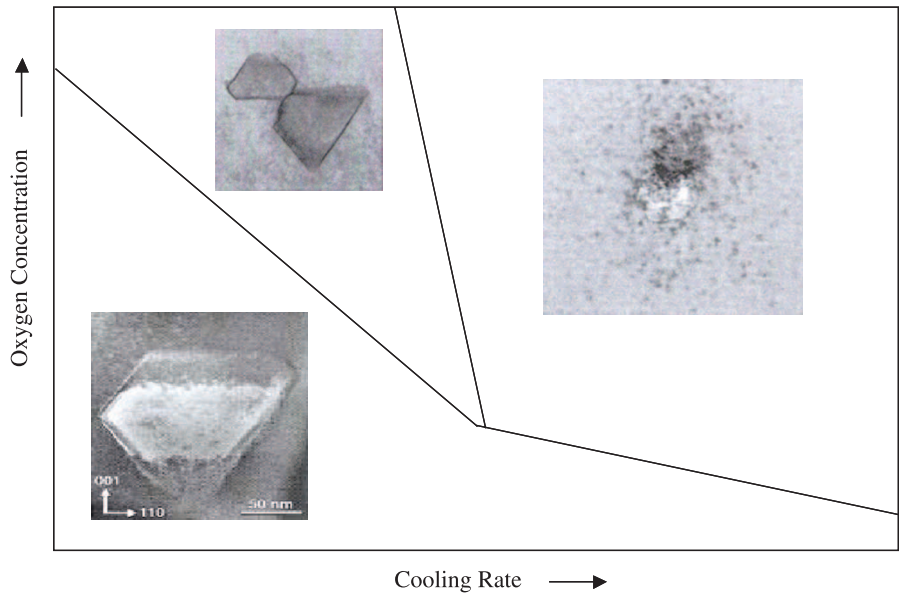

Figure 15. "Phase diagram" for void morphology as a function of oxygen concentration and crystal cooling rate during vacancy aggregation.

cloud-like void morphology found recently in OFZ and the more common double void structure found in CZ crystals are influenced strongly by the presence of oxygen, which binds to vacancies during crystal growth. Whether this binding affects the final void morphology or not depends also on the details of the crystal growth process parameters, particularly the time-temperature history. A summary "phase-diagram" of void morphology dependence on oxygen concentration and crystal cooling rate is shown in figure 15. At low oxygen concentrations, void growth is unaffected by interactions with oxygen and the final oxide coating is formed after the void size distribution is established. As the oxygen concentration increases, two possible interaction pathways can be activated. If the crystal-cooling rate is slow and the vacancy population does not become significantly supersaturated, interstitial oxygen atoms do not bind with single vacancies but do oxidize the surfaces of still-evolving voids, leading to double and triple void structures. However, if a vacancy supersaturation is present because of rapid cooling, which is present in OFZ crystal growth, then oxygen–vacancy complexes can form depleting the free vacancy population and destabilizing existing voids, which then begin to dissolve.

It should be noted that some of the conclusions presented in this paper were obtained somewhat indirectly on the basis of a constant-temperature LKMC model. While the effect of oxygen concentration was modeled explicitly, the effect of cooling rate during crystal growth was simulated indirectly by modifying the vacancy supersaturation and the simulation initial conditions. Future work is being applied towards the development of a variable temperature LKMC model which will enable more direct comparisons to defect evolution during actual processing conditions.

Acknowledgements

We gratefully acknowledge partial financial support from the National Science Foundation (CTS01-34418) and the Department of Chemical and Biomolecular Engineering at the University of Pennsylvania. We also thank Dr. Walter Haeckl and Dr. Wilfried von Ammon of Siltronic, AG (Germany) for valuable discussions regarding this work.

References

[1] J.B. Adams, Z.Y. Wang, Y.H. Li. Modeling Cu thin film growth. *Thin Solid Films*, **365**, 201 (2000).
[2] R. Pinacho, P. Castrillo, M. Jaraiz, I. Martin-Bragado, J. Barbolla, H.J. Gossmann, G.H. Gilmer, J.L. Benton. Carbon in silicon: modeling of diffusion and clustering mechanism. *J. Appl. Phys.*, **92**, 1582 (2002).
[3] O. Biham, I. Furman, M. Karimi, G. Vidali, R. Kennett, H. Zeng. Models for diffusion and island growth in metal monolayers. *Surf. Sci.*, **400**, 29 (1998).
[4] L.G. Wang, P. Clancy. Kinetic Monte Carlo simulation of the growth of polycrystalline Cu films. *Surf. Sci.*, **473**, 25 (2001).
[5] A. La Magna, S. Coffa, L. Colombo. A lattice kinetic Monte Carlo code for the description of vacancy diffusion and self-organization in Si. *Nucl. Instr. Meth. Phys. Res. B*, **148**, 262 (1999).
[6] J. Dai, J.M. Kanter, S.S. Kapur, W.D. Seider, T. Sinno. On-lattice kinetic Monte Carlo simulations of point defect aggregation in entropically influenced crystalline systems. *Phys. Rev. B*, **72**, 134102 (2005).
[7] J. Dai, W.D. Seider, T. Sinno. Lattice kinetic Monte Carlo simulations of defect evolution in crystals at elevated temperatures. *Mol. Simul.*, **32**, 305 (2006).
[8] J. Park, G. Rozgonyi. DRAM wafer qualification issues: oxide integrity vs. D-defects, oxygen precipitates and high temperature annealing. *Solid State Phenom.*, **47–48**, 327 (1996).
[9] M. Prasad, T. Sinno. Internally consistent approach for modeling solid-state aggregation. I. Atomistic calculations of vacancy clustering in silicon. *Phys. Rev. B*, **68**, 045206 (2003).
[10] M. Prasad, T. Sinno. Internally consistent approach for modeling solid-state aggregation. II. Mean-field representation of atomistic processes. *Phys. Rev. B*, **68**, 045207 (2003).

[11] S.S. Kapur, M. Prasad, J.C. Crocker, T. Sinno. Role of configurational entropy in the thermodynamics of clusters of point defects in crystalline solids. *Phys. Rev. B*, **72**, 014119 (2005).
[12] R. Falster, V.V. Voronkov, F. Quast. On the properties of the intrinsic point defects in silicon: a perspective from crystal growth and wafer processing. *Phys. Stat. Sol. B*, **222**, 219 (2000).
[13] K. Nakamura, T. Saishoji, J. Tomioka. Formation mechanism of voids and oxide precipitates in silicon crystals. *4th Int. Symp. Adv. Sci. Technol. Silicon Mater.*, JSPS, Hawaii, FL, 22–26 November (2004).
[14] K. Nakai, A. Ikari, A. Huber, W. Kaeckl, W. von Ammon. Void formation mechanism in floating zone silicon crystal. *4th Int. Symp. Adv. Sci. Technol. Silicon Mater.*, JSPS, Hawaii, FL, 22–26 November (2004).
[15] T.A. Frewen, T. Sinno. Vacancy self-trapping during rapid thermal annealing of silicon wafers. *Appl. Phys. Lett.*, **89**, 191903 (2006).
[16] T.A. Frewen, S.S. Kapur, W. Haeckl, W. von Ammon, T. Sinno. A microscopically accurate continuum model for void formation during semiconductor silicon processing. *J. Cryst. Growth*, **279**, 258 (2005).
[17] T. Sinno, R.A. Brown. Modeling microdefect formation in Czochralski silicon. *J. Electrochem. Soc.*, **146**, 2300 (1999).
[18] E. Dornberger. Prediction of OSF ring dynamics and grown-in voids in Czochralski silicon crystals. Ph.D. thesis, Universite Cath. De Louvain (1997).
[19] V. Voronkov. The mechanism of swirl defects formation in silicon. *J. Cryst. Growth*, **59**, 625 (1982).
[20] T. Sinno, R.A. Brown, W. von Ammon, E. Dornberger. Point defect dynamics and the oxidation-induced stacking-fault ring in Czochralski-grown silicon crystals. *J. Electrochem. Sco.*, **145**, 302 (1998).
[21] J. Vanhellemont, E. Dornberger, J. Esfandyari, G. Kissinger, M.A. Trauwaert, H. Bender, D. Graf, U. Lambert, W. von Ammon. Defects in as-grown silicon and their evolution during heat treatments. *Mater. Sci. Forum*, ICDS 19 (1997).
[22] M. Itsumi. Octahedral void defects in Czochralski silicon. *J. Cryst. Growth*, **237–239**, 1773 (2002).
[23] V.V. Voronkov. Formation of voids and oxide particles in silicon crystals. *Mater. Sci. Eng. B*, **73**, 69 (2000).
[24] V.V. Voronkov, R. Falster. Diffusion-limited growth of single- and double-octahedral voids in silicon and the effect of surface oxygen monolayer. *J. Cryst. Growth*, **226**, 192 (2001).
[25] M.Z. Bazant, E. Kaxiras, J.F. Justo. Environmental-dependent interatomic potential for bulk silicon. *Phys. Rev. B*, **56**, 8542 (1997).
[26] R.C. Newman. *Early Stage of Oxygen Precipitation in Silicon*, R. Jones (Ed.), , Kluwer Academic Publishers, Dordrecht (1996).
[27] R.A. Casali, H. Rucker, M. Methfessel. Interaction of vacancies with interstitial oxygen in silicon. *Appl. Phys. Lett.*, **78**, 913 (2001).
[28] M. Pesola, J. von Boehm, T. Mattila, R.M. Nieminen. Computational study of interstitial oxygen and vacancy–oxygen complexes in silicon. *Phys. Rev. B*, **60**, 11449 (1999).
[29] J.C. Mikkelsen. Oxygen,carbon, hydrogen, and nitrogen in silicon. *Mater. Res. Soc. Symp. Proc.*, Princeton, NJ 19 (1986).
[30] J. Vanhellemont. Diffusion limited oxygen precipitation in silicon: precipitate growth kinetics and phase formation. *J. Appl. Phys.*, **78**, 4297 (1995).
[31] J. Vanhellemont. On the impact of interface energy and vacancy concentration on morphology changes and nucleation of silicon oxide precipitates in silicon. *Appl. Phys. Lett.*, **68**, 3413 (1996).
[32] T.A. Frewen, T. Sinno, W. Haeckl, W. von Ammon. A systems-based approach for generating quantitative models of microstructural evolution in silicon materials processing. *Comput. Chem. Eng.*, **29**, 713 (2005).
[33] I.M. Lifshitz, V.V. Slyozov. The kinetics of precipitation from supersaturated solid solutions. *J. Phys. Chem. Solids*, **19**, 35 (1961).